PCCP

Impact of anion shape on Li+ solvation and on transport properties for lithium-air batteries: a molecular dynamics study

SCHOLARONE™
Manuscripts

PCCP

ARTICLE TYPE

Impact of anion shape on Li$^+$ solvation and on transport properties for lithium-air batteries: a molecular dynamics study†

Juliane Fiates^{a,b}, Yong Zhang^b, Luís F. M. Franco^a, Edward J. Maginn^b and Gustavo Doubek^a

Lithium-air batteries emerge as an interesting alternative for advanced energy storage devices. The complexity of such systems imposes great challenges. One of them resides in the selection of the pair lithium salt/solvent. Many electrolyte properties affect the operation of the batteries. Among these, transport properties and structural features have a special place. Via molecular dynamics simulations, we have calculated solution viscosity, ionic diffusivities and conductivities, as well as structural information, for two different salts in dimethyl sulfoxide (DMSO): lithium hexafluorophosphate - LiPF$_6$, and lithium pyrrolidine - LiPyr, at different temperatures and salt molalities. We show that, despite similar ionic transport properties, Li$^+$ solvation in the different salts is significantly different. Therefore, solutions with different solvation properties, which impact the overall battery performance, might present analogous ionic dynamics.

1 Introduction

Metal-air batteries are getting increasing attention for the position they can occupy as one of the most relevant energy storage devices in the future. When compared to the traditional Li-Ion, metal-air batteries can achieve up to 10 times higher energy density[1]. The complexity in designing and operating such devices, however, presents considerable challenges[2].

Among all possible metal anodes of a metal-air battery, lithium has always been contemplated as a good candidate[3]. Due to its high reactivity in aqueous solution, an aprotic electrolyte is preferred[4]. The aprotic Li-O$_2$ battery, composed by a lithium anode and a porous oxygen cathode, basically consists of lithium peroxide (Li$_2$O$_2$) reactions of formation and decomposition[5]. The electrolyte plays a crucial role in the system performance, as it constitutes the medium for reactants transport between cathode and anode during the charge and discharge processes[6]. Therefore, a deep understanding of the ionic transport properties, such as ionic conductivity, diffusivity, and viscosity, in a certain electrolyte, is necessary for an optimum electrolyte selection. Moreover, an ideal electrolyte for lithium-oxygen batteries should have high lithium ion conductivity, but also low volatility, and high oxygen solubility[2,7].

DMSO (dimethyl sulfoxide) emerges as a solvent able to fulfill

those features. Having a high donor number, DMSO has favorable interactions with cations[8]. The lithium salt, however, can also have an impact on the electrolyte stability[9]. Even being extensively used in commercial Li-ion batteries, LiPF$_6$ has several limitations such as chemical and thermal instability. Therefore, the anion selection opens the possibility to tune electrochemical systems[9,10].

To characterize the electrolyte behavior, and its transport properties, analysis of transference number and solvation distribution should be employed[9]. The solvation shell analysis is extremely important to understand the complex formation between cation, anion, and solvent, making possible the determination of the amount of "free" Li$^+$, which has a direct relation with Li-reactions[8,11].

Kirshnamoorthy et al.[12] have studied the impact of two anions (TFSI$^-$ (bis(trifluoromethane)sulfonimide) and BF$_4^-$ (tetrafluoroborate)) on the transport and structural properties of adiponitrile solutions. The authors have observed similar Li$^+$ solvation with both anions. The transport properties, however, have shown completely different behavior, which was justified by the solvation shell around the anions.

Burke et al.[5] evaluated the relation between anions and the reaction pathway for Li-air batteries. The authors concluded that the anion donor number impacts the solubility of the intermediate products. This solubility is related to Li$^+$ solvation, showing that high donor number anions can enhance the battery capacity and rechargeability. These results also depend on the solvent choice. For high donor number solvents, such as DMSO, this effect is less pronounced. The oxygen mobility in high donor number solvents is totally independent of the anion[2]. Despite this, larger anions

^{a} School of Chemical Engineering, University of Campinas, Campinas 13083-852, Brazil. Fax: +55193521-3910; Tel: +55193521-3944; E-mail: doubek@feq.unicamp.br
^{b} Department of Chemical and Biomolecular Engineering, University of Notre Dame, Notre Dame, Indiana 46556, USA. E-mail: ed@nd.edu

increase the availability of oxygen, which impacts the reactions; the superoxide intermediate may become less stable because of the large solvation structure caused by superoxide-anion coordination[2]. The synergy between anion concentration and O_2 solubility in DMSO was observed by Lindberg *et al.*[13]. Experimental measurements of $TFSI^-$ showed that increasing its concentration increases the solubility of O_2. Nevertheless, higher concentrations of ClO_4^- (perchlorate) and Tf^- (trifluoromethanesulfonate) leads to lower O_2 solubility.

The relation between Li^+ and anion has been also reported in some studies based on molecular simulations. The pair interaction between Li^+ and PF_6^- in propylene carbonate is weaker than between Li^+ and BF_4^-. The interaction also impacts viscosity, which achieves higher values in $LiBF_4$ solution at higher concentrations, corroborating the connected mobility of cation and anion[14]. Jones *et al.*[15] have investigated $LiBF_4$ in propylene carbonate/ethylene carbonate. The cation is solvated by propylene carbonate, and the anion by ethylene carbonate. At high salt concentration, the mobility of Li^+ and BF_4^- remains uncorrelated.

In the present study, we seek to investigate, through molecular dynamics simulations, if it is possible to relate the ionic transport properties and the structural aspects of the ionic solvation. We have chosen to study two different lithium salts in DMSO solutions: $LiPF_6$ and LiPyr. Literature with experimental data for thermophysical properties of DMSO solutions containing $LiPF_6$ or LiPyr, varying temperature and salt molality, is rather scarce. Aminabhavi and Gopalakrishna[16] have experimentally measured density and viscosity of pure DMSO at 25°C as 1096 kg·m^{-3} and 1.948 mPa·s, respectively. Lindberg *et al.*[13] have found a value of 2.14 mPa·s for the viscosity of pure DMSO at 22°C. For 0.1 M $LiPF_6$ in DMSO, Laoire *et al.*[17] reported an ionic conductivity of 0.211 S·m^{-1}. Recently, Elabyouki *et al.*[18] have calculated, using molecular dynamics simulations, the transport properties of 1.5 M $LiPF_6$ in DMSO in a hierarchical carbon electrode. They have calculated the Li^+ and the PF_6^- diffusion coefficients in the confinement direction. The values of diffusion coefficients in confinement media are known to be different than the unconfined values[19,20].

Electrolyte selection is a critical step for an optimum design of a lithium-air battery. We hope that testing the hypothesis of a possible relation between ionic transport and solution structure might help elucidate how these properties can guide a rational electrolyte selection.

2 Computational details

2.1 Force Fields

The chosen force fields are based on a sum of Lennard-Jones (LJ) and Coulombic potentials for nonbonded interactions. Equation 1 shows the total potential energy functional form, adding the bonded interactions:

$$U_{\text{total}} = \sum_{\text{bonds}} k_b (b - b_0)^2 + \sum_{\text{angles}} k_\theta (\theta - \theta_0)^2$$

$$+ \sum_{\text{dihedrals}} k_\phi [1 + \cos(n\phi - \delta)]$$

$$+ \sum_{\text{improper}} k_\psi [1 + \cos(n\psi - \delta)]$$

$$+ \sum_{i>j} \left\{ \frac{q_i q_j}{4\pi\varepsilon_0 r_{ij}} + 4\varepsilon_{ij} \left[\left(\frac{\sigma_{ij}}{r_{ij}} \right)^{12} - \left(\frac{\sigma_{ij}}{r_{ij}} \right)^6 \right] \right\} \quad (1)$$

where the total energy is expressed in terms of bond length, b, bond angle, θ, dihedral torsion angle, ϕ, and improper dihedral torsion angle, ψ; k is the constant related to each type of intramolecular force, q is the atomic charge related to the Coulombic electrostatic interactions, ε_0 is the vaccum permittivity, σ_{ij} and ε_{ij} are LJ potential parameters. Crossed LJ parameters were obtained applying Lorentz-Berthelot combining rules.

Atomistic representations of DMSO, Li^+, PF_6^-, and Pyr^-, are shown in Figure 1. The parameters used to simulate dimethyl sulfoxide (DMSO) were taken from a flexible all-atom model developed by Strader and Feller[21]. For $LiPF_6$, bond parameters of PF_6^- were taken from Kumar and Seminario[22], and nonbond parameters from Jorn *et al.*[23]. For LiPyr, both bond and nonbond parameters were taken from Liu and Maginn[24].
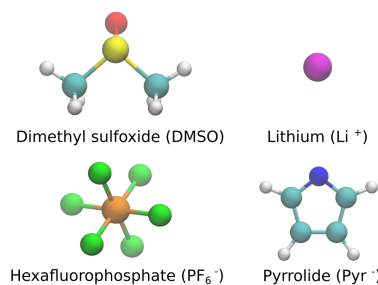

Fig. 1 All-atom representations of DMSO, Li^+, PF_6^-, and Pyr^-. Color code: oxygen (red), sulfur (yellow), carbon: (cyan), hydrogen: (white), lithium (magenta), phosphorus (orange), fluorine (green), and nitrogen (blue).

2.2 Molecular Dynamics Simulations

The initial configurations were assembled in a cubic box using the Packmol[25] package. We investigated four molalities: [0.25, 0.50, 0.75, 1.00] mol·kg^{-1} for both systems. The number of particles were fixed as $N_{\text{cation}} = N_{\text{anion}}/N_{\text{DMSO}}$: [40/2047, 40/1023, 40/682, 40/512], respectively. The same system size was applied to $LiPF_6$ and LiPyr in DMSO solutions.

All simulations were performed using LAMMPS[26]. The equilibration was carried out in the isothermal-isobaric ensemble (NPT) for 2 ns, followed by a production stage in the canonical ensemble (NVT) (for equilibration purposes 1 ns of NVT was run and ignored before the production starts). A Nosé-Hoover thermostat[27,28] and Parrinello-Rahman barostat[29] were

employed. Electrostatic interactions were computed using the particle-particle particle-mesh scheme (PPPM)[30]. For Lennard-Jones interactions, long-range corrections for energy and pressure were applied beyond a cutoff radius of 12 Å. Periodic boundary conditions were applied in all directions.

The production runs were carried out for 10 ns for the viscosity calculations, and 1 ns for diffusivity and conductivity calculations. Thermodynamic properties, and trajectories, were stored every 5 fs. The simulation length and recording times were selected based on literature recommendations[31,32] and preliminary tests. Radial distribution functions were obtained from the RDF subroutine implemented in LAMMPS. Densities were extracted directly from LAMMPS, as averages of NPT runs after 1.5 ns of equilibration. The standard deviations were evaluated considering 30 independent trajectories. More details can be found in an example input file provided in the supplementary material.

2.3 Transport Properties Calculation

Shear viscosities were calculated with the following Green-Kubo relation[33,34]:

$$\eta = \frac{V}{k_B T} \int_0^{+\infty} \langle P_{\alpha\beta}(t_0 + t) \cdot P_{\alpha\beta}(t_0) \rangle dt \quad (2)$$

where η is the shear viscosity, V is the system volume, k_B is the Boltzmann constant, T is the absolute temperature, $P_{\alpha\beta}$ is an independent component of the pressure tensor, and t is time. To improve the statistics of the calculation, additional independent components of the pressure tensor were used $(P_{xx} - P_{yy})/2$, $(P_{yy} - P_{zz})/2$, and $(P_{xx} - P_{zz})/2$[35].

Due to the large statistical uncertainty in viscosity calculation, the time decomposition method[32] was implemented. Using different velocity seeds, 30 independent trajectories were generated for each temperature and molality. The viscosity was then calculated using Equation 2. The averaged viscosity over the 30 trajectories was fitted to an empirical expression (Eq. 3[36,37]) using a weighting function $(1/t_b)$ up to a cutoff point.

$$\eta(t) = A\alpha\tau_1 \left(1 - e^{-t/\tau_1}\right) + A(1-\alpha)\tau_2 \left(1 - e^{-t/\tau_2}\right) \quad (3)$$

where $\eta(t)$ is the shear viscosity, A, α, τ_1, and τ_2 are fitting parameters. The cutoff point was established as the point for which the standard deviation of the average viscosity ($\sigma_{sd}(t)$ - Eq. 4) equals 40% of the viscosity value ($\langle \eta(t) \rangle$)[32]. In Equation 4, m is the number of trajectories:

$$\sigma_{sd}(t) = \sqrt{\frac{1}{m-1} \sum_{i=1}^{m} (\eta(t)_i - \langle \eta(t) \rangle)^2} \quad (4)$$

The weighting parameter b was obtained fitting the standard deviation to a power law function, as shown in Equation 5[32].

$$\sigma_{sd}(t) = Ct^b \quad (5)$$

where $\sigma_{sd}(t)$ is the standard deviation and C and b are fitting parameters.

The error was estimated as[36,37]:

$$\Delta\eta = \sqrt{\frac{2A[\alpha\tau_1 + (1-\alpha)\tau_2]}{t_{max}}} \quad (6)$$

where t_{max} is the maximum decay time.

Self-diffusion coefficients were calculated using a Green-Kubo relation, which is completely analogous to the Einstein-Smoluchowski approach[38]. Equation 6 shows the Green-Kubo relation for self-diffusion coefficient calculation as the time integral of the velocity autocorrelation function (VACF)[33,34].

$$D_i = \frac{1}{3N_i} \int_0^{+\infty} \sum_{k=1}^{N_i} \langle \mathbf{v}_k(t_0 + t) \cdot \mathbf{v}_k(t_0) \rangle dt \quad (7)$$

where D_i is the diffusion coefficient of ionic species i, N_i is the total number of ions i, the angle brackets represent the ensemble average of the velocity correlation over all time origins, and $\mathbf{v}_k$ is the velocity of ion k.

As for viscosity, the diffusivity calculation is also subjected to statistical estimation uncertainty[31,37]. Thus, ten independent trajectories were used, and the averaged diffusivity was fitted to an exponential function:

$$D(t) = D + a\exp(-bt) \quad (8)$$

where D, a, and b are fitting parameters. The standard deviation was obtained from the average of all trajectories. The diffusion is highly affected by the system size[31,38,39]. Therefore, we applied in our calculations a correction for system-size effects as follows[39-41]:

$$D_\infty = D_{PBC} + \frac{2.837297 k_B T}{6\pi\eta L} \quad (9)$$

where D_∞ is the diffusion coefficient in an infinite system, D_{PBC} is the diffusion coefficient calculated using periodic boundary condition, and L is the cubic box length.

The ionic conductivity was calculated by the electrical current autocorrelation function as[37]:

$$\sigma = \frac{1}{3k_B T V} \int_0^{+\infty} \langle \mathbf{J}(t_0 + t) \cdot \mathbf{J}(t_0) \rangle dt \quad (10)$$

where σ is the ionic conductivity, and the electrical current, $\mathbf{J}$, is obtained by the product between the ionic charge, q_i, and its velocity, $\mathbf{v}_i$, computed over all the N molecules:

$$\mathbf{J} = \sum_{i=1}^{N} q_i \mathbf{v}_i \quad (11)$$

In the conductivity calculation, the same number of trajectories, and the same fitting procedure described for the diffusivity calculation, were adopted.

3 Results and discussion

3.1 Density

Figure 2 shows the solution density of LiPF$_6$ and LiPyr in DMSO at 298 K and 1 atm as a function of salt molality. The effect of the salt molality on the solution density is more pronounced for

LiPF$_6$ in DMSO. Since Pyr$^-$ is planar and PF$_6^-$ is spherical, the structural arrangement in each system is different (as shown later in Figs 9 and 10), which has impacts on the total volume. Also, the mass of PF$_6^-$ is almost twice the mass of Pyr$^-$. Therefore, the increment in the number of PF$_6^-$ ions has a larger effect on the solution density.
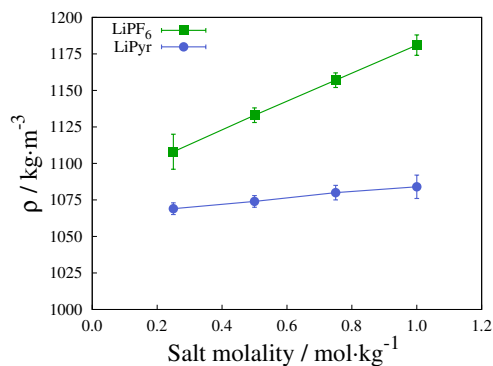

Fig. 2 Density of LiPF$_6$ and LiPyr in DMSO solutions as a function of salt molality at 298 K and 1 atm.

The temperature dependence of the density for 1 mol·kg^{-1} solutions is shown in Table 1. As temperature increases, the density slightly decreases for both systems. The thermal expansion coefficient was calculated from its definition [42,43]:

$$\alpha_P = -\frac{1}{\rho}\left(\frac{\partial \rho}{\partial T}\right)_P \qquad (12)$$

Both systems have a positive thermal expansion coefficient at these conditions: 8.60×10^{-4} K^{-1} for LiPF$_6$, and 9.97×10^{-4} K^{-1} for LiPyr. Densities of pure DMSO are shown in Figure 3. The simulations slightly underestimate the density of pure DMSO. The calculated thermal expansion coefficient at 298 K is 8.60×10^{-4} K^{-1} and, the experimental value reported in the literature is 9.13×10^{-4} K^{-1} [43].

Table 1 Density of 1 mol·kg^{-1} LiPF$_6$ in DMSO solution, and of 1 mol·kg^{-1} LiPyr in DMSO solution, as a function of temperature at 1 atm.

Temperature / K	Density / kg·m^{-3}	
	LiPF$_6$ in DMSO	LiPyr in DMSO
298	1181 ± 7	1084 ± 8
330	1147 ± 7	1051 ± 7
360	1118 ± 7	1017 ± 8

3.2 Transport Properties

Figure 4 shows the shear viscosity at 1 atm of LiPF$_6$ and LiPyr in DMSO as a function of salt molality at 298 K and as a function of temperature at a molality of 1 mol·kg^{-1} (Figure S1 presents the fitting of shear viscosity for both systems at 1 mol·kg^{-1} and 298 K). The shear viscosity increases with salt molality for both salts. A similar behavior has been reported for LiBF$_4$ in propylene carbonate [15]. As expected for liquids, the shear viscosity of the solution decreases with increasing temperature for both salts.
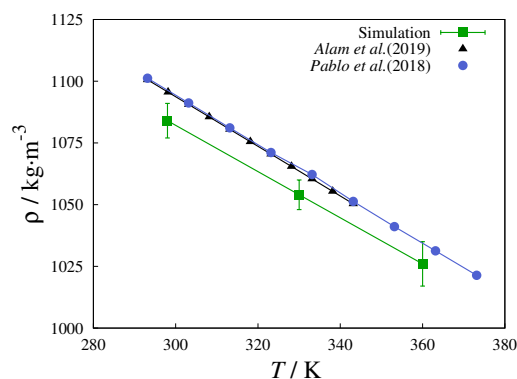

Fig. 3 Density of pure DMSO as a function of temperature at 1 atm. Experimental measurements were taken from literature [43,44].

Being consistently less viscous within the studied range of conditions, LiPyr in DMSO solutions present higher mobility than solutions of LiPF$_6$ in DMSO. The calculated viscosity values for pure DMSO are in excellent agreement with experimental data, suggesting that the force field for DMSO is adequate to represent the transport properties of such a system.

The ionic diffusion coefficients for Li$^+$, PF$_6^-$, and Pyr$^-$ in DMSO solutions are shown in Figure 5 (Figure S2 presents the fitting of self-diffusion coefficients for cations and anion of both systems at 1 mol·kg^{-1} and 298 K). Diffusion coefficients decrease with increasing salt molality since more crowded systems have less available free space. This behavior has already been noticed in similar systems [14,15]. On the other hand, diffusion coefficients increase with temperature since the probability of achieving higher velocities is enhanced at higher temperatures. A system size analysis over diffusivity can be found in Section 2 of ESI†.

Within the statistical uncertainty, the anions of both salts have essentially the same diffusion coefficients. Nevertheless, although Li$^+$ ions are much smaller than the anions, they have lower diffusion coefficients than the anions, and such coefficients remain unaffected by the anion type. Regarding the solvent, DMSO has higher mobility in composition with LiPyr (Fig. 5 (b)) agreeing with the viscosity profile showed in Figure 4 (b). Moreover, a smaller presence of DMSO in Li$^+$ solvation shell is observed for LiPyr (Fig. 10), which is probably enhancing DMSO mobility.

The effects of salt molality and temperature on the ionic conductivity of LiPF$_6$ and LiPyr in DMSO solutions are shown in Figure 6 (Figure S3 illustrates the fitting of conductivity for both systems at 1 mol·kg^{-1} and 298 K). A good agreement is observed with experimental data [17,45] for LiPF$_6$ at molalities of 0.1 and 1.0 mol·kg^{-1} (Fig. 7(a)), indicating that the force field is able to capture the behavior of this system. A nonlinear increase of ionic conductivity with increasing salt molality is observed. A similar trend was experimentally observed for DMSO solutions of LiTFSI, LiClO$_4$, and LiTf [13]. The salt type seems to have a negligible effect on the computed ionic conductivities presented here, and this result corroborates what was experimentally observed for other lithium salts in DMSO solutions. As with the diffusion coefficients, the ionic conductivity values are higher for higher
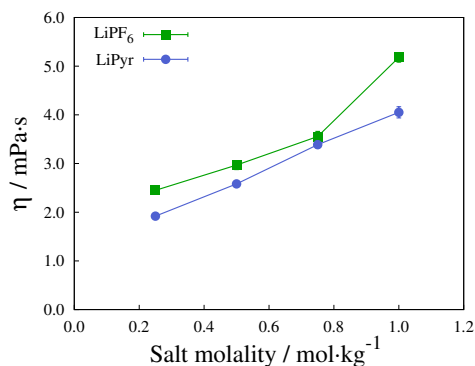
(a)
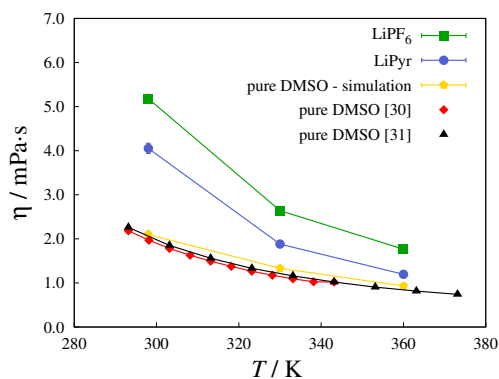
(b)

Fig. 4 Shear viscosity of LiPF$_6$ and of LiPyr in DMSO solutions at 1 atm as a function of: (a) salt molality at 298 K, and (b) temperature for solutions with 1 mol·kg^{-1} (simulation and experimental[43,44] values for pure DMSO are also shown for comparison purposes). Uncertainties are on the order of $\pm$ 0.1 mPa·s for all simulated results.

(a)

(b)

Fig. 5 Self-diffusion coefficients of Li$^+$ and PF$_6^-$ in DMSO solution of LiPF$_6$, and of Li$^+$ and Pyr- in DMSO solution of LiPyr, at 1 atm as a function of: (a) salt molality at 298 K, and (b) temperature for solutions with 1 mol·kg^{-1} (The self-diffusion coefficients of DMSO in the salt solutions are also shown). The error bars at the lowest temperature are smaller than the symbol size.

temperatures and independent of system size effect as shown in Section 2 of ESI†.

At infinite dilution, the ionic conductivity can be estimated from the Nernst-Einstein relation[46]:

$$\sigma_{NE} = \frac{1}{k_B T} \sum_{i=1}^{N} \rho_i q_i^2 D_i \quad (13)$$

where σ_{NE} is the Nernst-Einstein ionic conductivity, ρ_i is the number density of ion i, and D_i is the diffusion coefficient of ion i.

The relation between the ionic conductivity calculated by Green-Kubo approach and the Nernst-Einstein ionic conductivity can be expressed as:
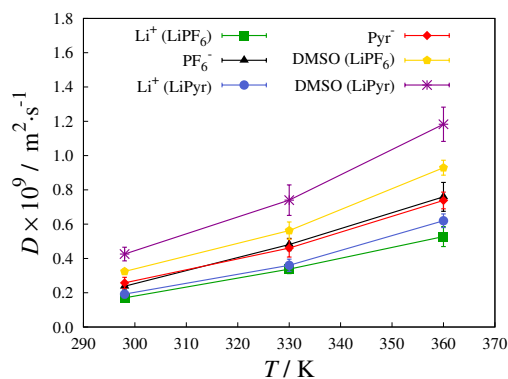
$$\sigma = \sigma_{NE} (1 - \Delta) \quad (14)$$

where Δ is the Nernst-Einstein deviation parameter, which can be defined in terms of the time integral of the velocity cross-correlation function for unlike ions[47]. Δ has been shown to be independent of temperature and pressure[48]. Here, we calculated Δ for different salt molalities and temperatures, as presented in Figure 7, and the results show that Δ seems to be independent of salt molality, as well as of temperature at the studied range.

A relation between the limiting molar ionic conductivity and

the viscosity was first proposed by Walden[49]. The Walden's rule states that the product between these two properties should be constant:

$$\Lambda \eta = \text{constant} \quad (15)$$

where Λ is the limiting molar ionic conductivity defined in terms of the Nernst-Einstein ionic conductivity for 1:1 electrolytes as:

$$\Lambda = \frac{\sigma_{NE}}{c} \quad (16)$$

where c is the electrolyte molar concentration.

This rule can be derived assuming the validity of Stokes-Einstein relation for the ionic diffusivity:

$$D_i = \frac{k_B T}{6\pi \eta r_i} \quad (17)$$

where r_i is the Stokes radius of ion i.

Substituting Equations (16) and (17) into Equation (15), one has that for a 1:1 electrolyte:

$$\Lambda \eta = \frac{e^2 N_A}{6\pi} \left[\frac{1}{r^+} + \frac{1}{r^-} \right] \quad (18)$$

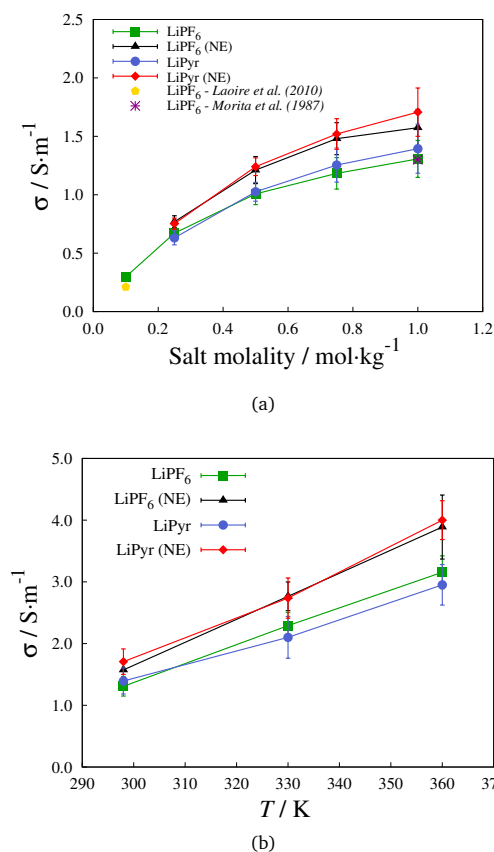where e is the elementary charge, N_A is the Avogadro's number,

(a)

(b)

Fig. 6 Ionic conductivity of LiPF$_6$ and LiPyr in DMSO solutions at 1 atm as a function of: (a) salt molality at 298 K (experimental data values for concentrations of 0.1 mol·kg^{-1} [22] and 1 mol·kg^{-1} [45] of LiPF$_6$ in DMSO are also presented), and (b) temperature for solutions with 1 mol·kg^{-1}. Nernst-Einstein (NE) ionic conductivities are shown for comparison purposes. The uncertainties for NE ionic conductivities were propagated from the uncertainties of the corresponding diffusion coefficients. The error bars at the lowest temperature are smaller than the symbol size.

r^+ is the cation Stokes radius, and r^- is the anion Stokes radius.

Therefore, Walden's rule is satisfied provided Nernst-Einstein and Stokes-Einstein relations are valid.

Although the conclusions on ion-pairing and association exclusively obtained from a direct analysis of the so-called Walden plot (log Λ *versus* log η^{-1}) have been vehemently criticized [50] in the case of ionic liquids, especially when compared to the arbitrary reference of the ideal aqueous KCl line [51], a simple observation of the Walden plot might help to classify different electrolytes in terms of the combination between the ionic conductivity and the solution viscosity.

Figure 8 presents the Walden plot for LiPF$_6$ and LiPyr in DMSO solutions, calculated using both the ionic conductivity and the Nernst-Einstein ionic conductivity for different temperatures. As expected, the Nernst-Einstein deviation parameter is independent of temperature. Both solutions have similar transport properties and the only significant difference is in viscosity. DMSO solutions of LiPyr are less viscous, and therefore their data are shifted to the right in the Walden plot in comparison to DMSO solutions of LiPF$_6$.
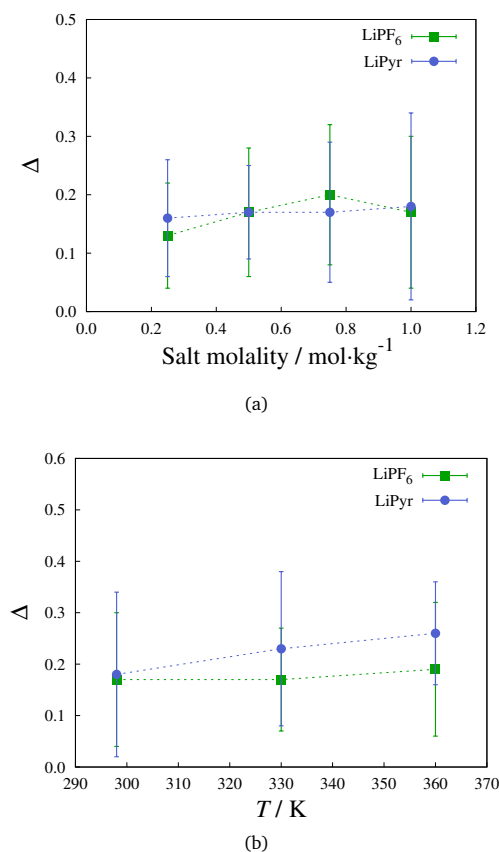

(a)

(b)

Fig. 7 The Nernst-Einstein deviation parameter, Δ, for LiPF$_6$ and LiPyr in DMSO solutions at 1 atm as a function of: (a) salt molality at 298 K, and (b) temperature for solutions with 1 mol·kg^{-1}. The uncertainties were propagated from the uncertainties of the corresponding conduction coefficients.

In terms of Walden's rule, the slope of the curves in the Walden plot should be 1. Some systems, however, exhibit a different behavior, which has been treated with the fractional Walden rule [52]:

$$\Lambda \eta^{\alpha} = \text{constant} \tag{19}$$

where α is the Stokes-Einstein exponent [48].

Using Nernst-Einstein ionic conductivities, we found that $\alpha = 0.89$ for DMSO solutions of LiPF$_6$, and $\alpha = 0.74$ for DMSO solutions of LiPyr. The experimentally determined value for α for an infinitely diluted aqueous KCl solution is 0.87 [51].

From the transport properties viewpoint, no significant difference between DMSO solutions of LiPF$_6$ and LiPyr was observed. These solutions differ only in viscosity and in Stokes-Einstein exponents. Despite the differences in shape and composition, the ionic transport seems to be independent of the anion type in the present case.

3.3 Structural arrangement

To examine the structural arrangement of the solvated ions in DMSO, the radial distribution function (RDF), and the corresponding coordination number, n, calculated by the running integral of the RDF, are analyzed.
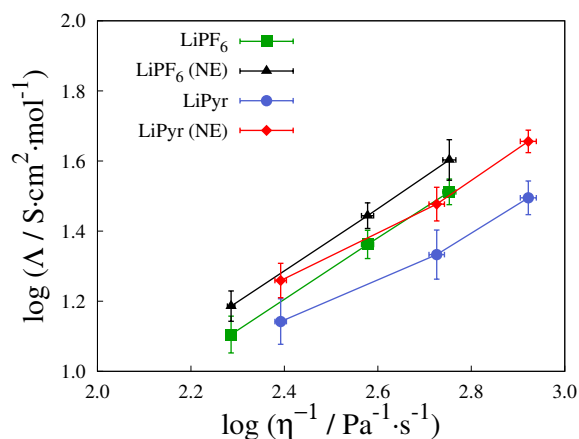
Fig. 8 Walden plot for LiPF$_6$ and LiPyr in DMSO solutions, using both calculated ionic conductivity and the calculated Nernst-Einstein (NE) ionic conductivity for different temperatures. Some error bars cannot be seen because they are smaller than the symbol size. Note the different scales in X and Y-axes.

Fig. 10 Radial distribution functions (RDF) (solid lines, left y axis), and coordination numbers (dashed lines, right y axis) for Li–O (DMSO) - red, Li–N(Pyr) - black, Li–H4(Pyr) - blue, and Li–Ha(Pyr) - green at 298 K and 1 atm for 1.0 mol·kg^{-1} DMSO solution of LiPyr. The inset plot shows the solvation structure of Li$^+$. The distances are in Angstrom. Atom color code: lithium (magenta), oxygen (red), nitrogen (blue), carbon (cyan), and hydrogen (white).

Figures 9 and 10 present the radial distribution functions between Li$^+$ and the DMSO oxygens, as well as Li$^+$ and PF$_6^-$ atoms (Fig. 9), and Li$^+$ with Pyr$^-$ hydrogen and nitrogen atoms (Fig. 10), all systems with 1 mol·kg^{-1} at 298 K and 1 atm. To understand the influence of molality and temperature on the Li$^+$ coordination shell behavior, we have determined the first layer, which corresponds to the minimum after the first peak: being 2.35 Å for O and F in PF$_6^-$, and 2.6 Å and 3.0 Å for O and N in Pyr$^-$, respectively. Figures S5 and S6 of ESI† present the RDF profiles for different molalities and temperatures for LiPF$_6$ and LiPyr, respectively. The inset plots of Figures 9 and 10 illustrate the shell configuration around Li$^+$.
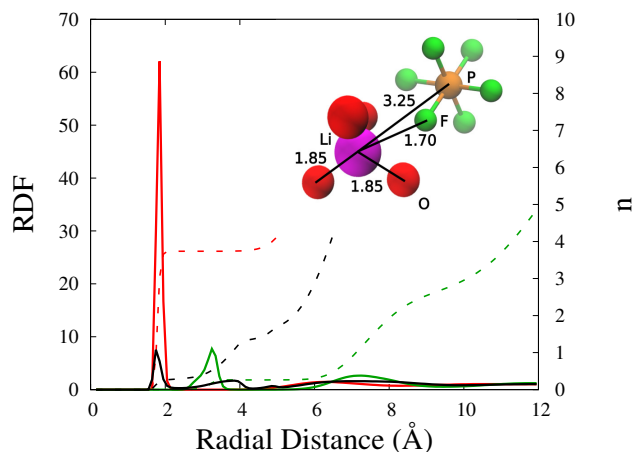

Fig. 9 Radial distribution functions (RDF) (solid lines, left y axis), and coordination numbers (dashed lines, right y axis) for Li–O (DMSO) - red. Li–F(PF$_6$) - black, and and Li–P(PF$_6$) - green at 298 K and 1 atm for 1.0 mol·kg^{-1} DMSO solution of LiPF$_6$. The inset plot shows the solvation structure of Li$^+$. The distances are in Angstrom. Atom color code: lithium (magenta), oxygen (red), phosphorus (orange), and fluorine (green).

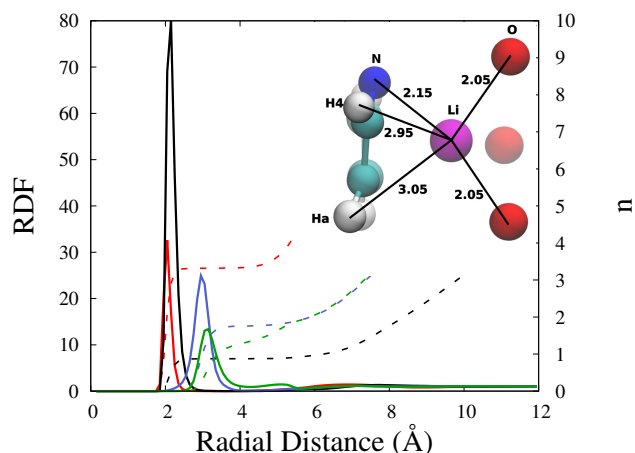Figure 11 (a) and (b) present the coordination number val-

ues as a function of molalities and temperatures (Table S1 of ESI†presents more information on coordination numbers). Lithium ions are highly coordinated with four oxygens in DMSO solutions of LiPF$_6$. This result is in agreement with the observation that lithium ion is solvated by four DMSO molecules forming Li$^+$(DMSO)$_4$PF$_6^-$ ion pair[53,54]. Yamada et al.[55] have also shown, with Raman spectroscopy, the Li$^+$(DMSO)$_4$ coordination in 1 mol·kg^{-1} solution, as can be seen in 11 (a). The preferential solvation of Li$^+$ by DMSO, even in acetonitrile-DMSO mixtures with low DMSO mole fractions, has been observed by experimental measurements of ionic conductivity[56]. Li$^+$ solvation in DMSO remains constant with increasing salt molality, and an analogous behavior is observed for the influence of temperature.

A different arrangement is found for LiPyr in DMSO solution. As shown in Figure 10, lithium ions are much more correlated with the anions. The values of coordination (Fig. 11 (a)) reveal higher ion pairing increasing with salt molality. In contrast, the number of DMSO solvating Li$^+$ decreases at high molalities. A persistent presence of ion contact, even at low molalities of LiPyr in DMSO solutions, is observed.

The negative charge in PF$_6^-$ is more delocalized in comparison with Pyr$^-$. In PF$_6^-$, the negative charge is distributed along all fluorine atoms, which weakens the electrostatic interaction between PF$_6^-$ and Li$^+$. The molecular arrangement of PF$_6^-$ also contributes to its lower interaction with Li$^+$. On the other hand, for Pyr$^-$ the negative charge is positioned mostly at nitrogen and close hydrogens (H4 - Fig. S8 of ESI†), which facilitates the interaction between Li$^+$ and Pyr$^-$. At high molalities, the ions are much more packed, increasing the probability of interaction of Li$^+$ and Pyr$^-$ by the electrostatic forces.

Regarding temperature, we found a slight increase in ion pairing and desolvation for Li$^+$ of LiPyr in DMSO solution at higher temperatures, as can be seen in Figure 11 (b). The opposite behavior happens for Li$^+$ of LiPF$_6$ in DMSO, where an increase of

solvation decreasing ion pair interaction at higher temperatures is found.

Figure 11 (c) shows the probability distribution for the Li$^+$ solvation for DMSO oxygen and phosphorus from PF$_6^-$, as well as nitrogen from Pyr$^-$ in solutions with 1.0 mol·kg^{-1} at 298 K. Figure S7 (a-e) of ESI† illustrates the environmental distribution for other molalities and at other temperatures. The average coordination profile is the most probable scenario of ion pair distribution, except for 0.25 mol·kg^{-1} at 298 K (Fig. S7 (a)), where the systems exhibits a higher probability of no ion pair coordination of Pyr$^-$ with Li$^+$, and a solvation shell composed by five DMSO molecules. For LiPF$_6$ in DMSO, a preference for the full solvation of Li$^+$ by four molecules of DMSO for all investigated molalities and temperatures is observed. This result highlights the tendency of Li$^+$ from LiPyr in DMSO to be partially coordinated by three DMSO molecules, and of keeping an ion pair coordination with the negative termini of Pyr, corroborating the theory of the impact of shape and charge distribution on the solvation sphere formation.

Since we have different solvation structures for each system, a question that emerges is how this impacts the mobility, and ultimately the ionic conduction, on these systems. Hence, the transference number of Li$^+$ (t^+) was calculated by the following expression [11,57,58] ($t^+ + t^- = 1$):

$$t^+ = \frac{D^+}{D^+ + D^-} \tag{20}$$

where D^+ and D^- are the diffusivity of cation and anion, respectively.

Figure 12 and Table 2 present the results for different molalities and at different temperatures. On both cases, a considerable influence of anion on the total charge transport is seen ($t^+ < 0.5$). This is caused by the packed solvation shell around Li$^+$ turning it heavier, and hence decreasing the ion mobility.

A closer look to Figure 12 shows a slightly higher transference number for LiPyr in comparison with LiPF$_6$ both in DMSO solvent solution. This result implies that, even though they have different solvation shell compositions, the size and motion are similar. Our results show good agreement with typical battery electrolytes, such as LiPF$_6$ and LiBF$_4$ in propylene carbonate [14], as well as for poly(allylglycidyl ether-lithium sulfonate) in DMSO solution [58]. Furthermore, in our findings, the transference number is almost independent of molality, but highly influenced by temperature for LiPyr (Table 2).

Table 2 The Li$^+$ transference number (t^+) for LiPF$_6$ and LiPyr in DMSO solutions with 1 mol·kg^{-1} at different temperatures at 1 atm, calculated from Green-Kubo diffusivity [a].

	Temperature / K		
	298	330	360
t^+ for LiPF$_6$ in DMSO	0.417	0.412	0.410
t^+ for LiPyr in DMSO	0.427	0.439	0.456

[a] Uncertainties are on the order of ± 0.0001 for all results. They were propagated from uncertainties of diffusion coefficients.

3.4 Consequences for Li-Air Battery

DMSO is a widely used solvent for Li-air batteries [7,59]. Having a high Donor Number (DN = 29.8), DMSO has the ability to donate free electron pairs to coordinate with acceptor atoms from ions in solution. DMSO also has high oxygen solubility, and high polarity [8,59,60]. These features confer to DMSO good interaction with positive ions as Li$^+$, contributing to the stability of intermediate products on Li-air reactions [59].

Nevertheless, Burke et al. [5] have shown that the anion DN can largely affect LiO$_2$ solubility, due to anion and Li$^+$ correlation. The authors evaluated two anion types: NO$_3^-$, which has a planar shape and high DN; and TFSI$^-$, which has ellipsoidal shape and low DN. The combination of high DN anion and low DN solvent DME (1,2-dimethoxyethane) provided good capacities and increased the stability of intermediate reaction products. Changing the solvent to DMSO (high DN), no improvement was observed.

In this work, we have analyzed two different salts (LiPF$_6$ and LiPyr) in DMSO solution. Our results indicate that the anion shape and charge distribution play important roles on the Li$^+$ solvation. For PF$_6^-$, which has low DN and a spherical shape [61], no impact on solvation of Li$^+$ was observed, being Li$^+$ fully solvated by DMSO. On the other hand, for Pyr$^-$, Li$^+$ is partially solvated by DMSO and, at same time, participates with Pyr$^-$ in ion pairing. Pyr$^-$ has a planar shape and, based on measures for other nitrogen-based anions [62], one can speculate Pyr$^-$ has a high DN. In NO$_3^-$, the negative termini position is at the three oxygens, and, in Pyr$^-$, it is located largely at the nitrogen and close hydrogens (H4 - Fig. S8 of ESI†). The high DMSO ability to solvate Li$^+$ decreases the possibility of NO$_3^-$ negative structure to interact with Li$^+$, due to oxygen partial charges. In Pyr$^-$ case, even in presence of DMSO solvent, the charge position facilitates Li$^+$ and Pyr$^-$ coordination.

A direct consequence of the solvation shell is the reaction path in the full cell evaluation. As reported by Gittleson et al. [2], the solvation of Li$^+$ is the major factor that impacts on the reaction mechanism. [5] The free energies of both Li$^+$ and LiO$_2$ are directly related to the Li$^+$ coordinated species. Their experimental measures show that ion-pairing formation induces the stability of the intermediate anion O$_2^-$ in solution, which increases the Li$_2$O$_2$ growth mechanism. The authors demonstrated that no ion-pairing was noticed in DMSO solutions of LiTFSI or LiNO$_3$.

Dilimon et al. [59] have evaluated the stability of superoxide formation in sodium-air batteries. The authors concluded that stabilization of superoxide formation is conditioned to the softness of Li$^+$ solvation shell. According to their findings, high DN solvent (DMSO) and high DN anion (SO$_3$CF$_3^-$) make the superoxide formation possible, which increases the battery reversibility. Abraham et al. [61] have shown that cation and anion coordination in the first solvation shell increases the softness on Li$^+$. And the co-participation of solvent and anion in solvation structure of cation is essential for superoxide stability [59]. Since Li$^+$ is a hard ion, the same as Na$^+$, a similar behavior is expected. The negative termini in SO$_3$CF$_3^-$ are predominantly at the external oxygens, the same as for nitrogen and its close hydrogens (H4 - Fig. S8 of

ESI†) in Pyr$^-$, which may justify the good interaction of $SO_3CF_3^-$ with Na$^+$.

As the solvation shell, the transference number (t^+) elucidates the impact of Li$^+$ mobility on charge transference process. Lower values of t^+ express a limited Li$^+$ motion. This limitation promotes concentration gradients that impacts the ion transfer when reaction with adsorbed O$_2$ in Li-air devices[11,57]. Our results show slightly higher transference numbers in comparison with typical carbonated solvents (Fig. 12). Regarding LiPF$_6$ and LiPyr in DMSO, LiPyr presented an averaged growth of 3.3% for molality and 6.2% for temperature on t^+ in comparison to LiPF$_6$. Higher values of t^+ are beneficial for the overall battery performance[57].

Despite similar ionic conductivities of the two selected anion shapes our results show that the coordination of them with the respective anion is very distinct. We hope that this information highlighted here might aid future experimental work investigating the stability of dissociated intermediaries such as LiO$_2$ with important consequences for the reaction pathway.

4   Conclusions

LiPF$_6$ and LiPyr in DMSO solutions constitute possible electrolyte candidates for Li-O$_2$ battery applications. Carrying out classical molecular dynamics simulations, Li$^+$ solvation and the transport properties of these solutions have been assessed.

Through the calculation of transport properties, such as viscosity, diffusion coefficient, and ionic conductivity, we concluded that the ionic transport is quite similar regardless of the anion type. The differences in the anion shape and composition, however, are sufficient to affect solution viscosity: LiPyr in DMSO solution is less viscous than LiPF$_6$ in DMSO.

The structural arrangement of these two solutions presents a completely different scenario. In LiPF$_6$/DMSO system, Li$^+$ is fully solvated by DMSO, and its coordination number with DMSO oxygen matches exactly what has been claimed in the literature for the formation of Li$^+$(DMSO)$_4$PF$_6^-$ ion pair[53]. In LiPyr/DMSO system, however, the Li$^+$ first solvation shell is partially shared between the solvent and the anion. Despite having different solvation shell, the transference number indicates that their volumes are similar.

The ionic dynamics of these solutions, as manifested in the computed transport properties, are similar, even though the Li$^+$ solvation in each solution is different. The selection of the pair lithium salt/solvent is essential for an optimum operation of a Li-O$_2$ battery, and many variables ought to be analyzed. In the present study, we have shown that similar transport behavior can be observed for solutions with different solvation properties, which might have a significant impact on reaction intermediate (LiO$_2$) solubility and therefore on the overall reaction mechanism. This conclusion might give insights for experimental design and analysis when addressing electrolyte impact over Li$-$O$_2$ devices.

## Conflicts of interest

There are no conflicts to declare.

References

1   G. Girishkumar, B. McCloskey, A. C. Luntz, S. Swanson and W. Wilcke, *J. Phys. Chem. Lett.*, 2010, **1**, 2193–2203.

2   F. S. Gittleson, R. E. Jones, D. K. Ward and M. E. Foster, *Energ. Environ. Sci.*, 2017, **10**, 1167–1179.

3   K. M. Abraham and Z. Jiang, *J. Electrochem. Soc.*, 1996, **143**, 1–5.

4   Y. Li and J. Lu, *ACS Energy Lett.*, 2017, **2**, 1370–1377.

5   C. M. Burke, V. Pande, A. Khetan, V. Viswanathan and B. D. McCloskey, *Proc. Natl. Acad. Sci. U.S.A*, 2015, **112**, 9293–9298.

6   S. Han, *Sci. Rep.*, 2019, **9**, 1–10.

7   F. S. Gittleson, R. C. Sekol, G. Doubek, M. Linardi and A. D. Taylor, *Phys. Chem. Chem. Phys.*, 2014, **16**, 3230.

8   J. Smiatek, A. Heuer and M. Winter, *Batteries*, 2018, **4**, year.

9   K. Xu, *Chem. Rev.*, 2014, **114**, 11503–11618.

10   K. Xu, *Chem. Rev.*, 2004, **104**, 4303–4417.

11   O. Borodin, L. Suo, M. Gobet, X. Ren, F. Wang, A. Faraone, J. Peng, M. Olguin, M. Schroeder, M. S. Ding, E. Gobrogge, A. Von Wald Cresce, S. Munoz, J. A. Dura, S. Greenbaum, C. Wang and K. Xu, *ACS Nano*, 2017, **11**, 10462–10471.

12   A. Narayanan Kirshnamoorthy, K. Oldiges, M. Winter, A. Heuer, I. Cekic-Laskovic, C. Holm and J. Smiatek, *Phys. Chem. Chem. Phys.*, 2018, **20**, 25701–25715.

13   J. Lindberg, B. Endródi, G. Åvall, P. Johansson, A. Cornell and G. Lindbergh, *J. Phys. Chem. C*, 2018, **122**, 1913–1920.

14   M. Takeuchi, Y. Kameda, Y. Umebayashi, S. Ogawa, T. Sonoda, S. ichi Ishiguro, M. Fujita and M. Sano, *J. Mol. Liq.*, 2009, **148**, 99–108.

15   R. E. Jones, D. K. Ward, F. S. Gittleson and M. E. Foster, *J. Electrochem. Soc.*, 2017, **164**, A1258–A1267.

16   T. M. Aminabhavi and B. Gopalakrishna, *J. Chem. Eng. Data*, 1995, **40**, 856–861.

17   C. Laoire, S. Mukerjee, K. M. Abraham, E. J. Plichta and M. A. Hendrickson, *J. Phys. Chem. C*, 2010, **114**, 9178–9186.

18   M. Elabyouki, D. Bahamon, M. Khaleel and L. F. Vega, *J. Phys. Chem. C*, 2019, **123**, 27273–27285.
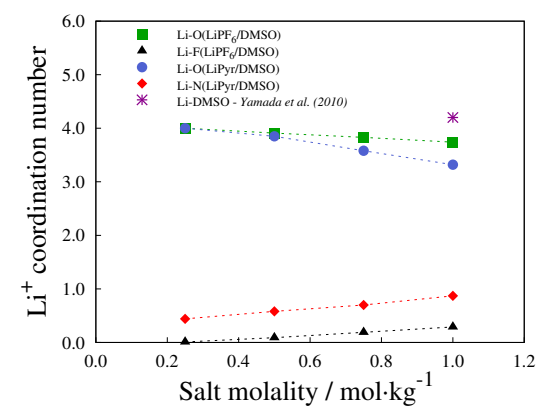
(a)
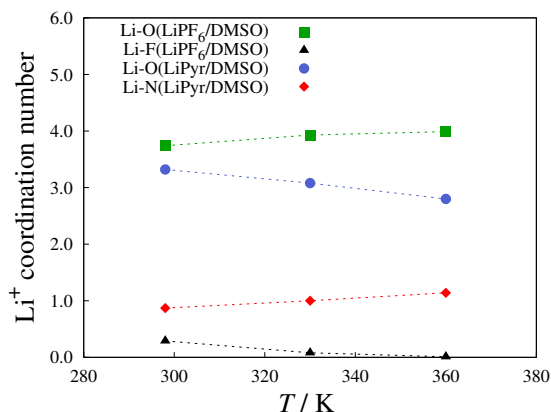
(b)
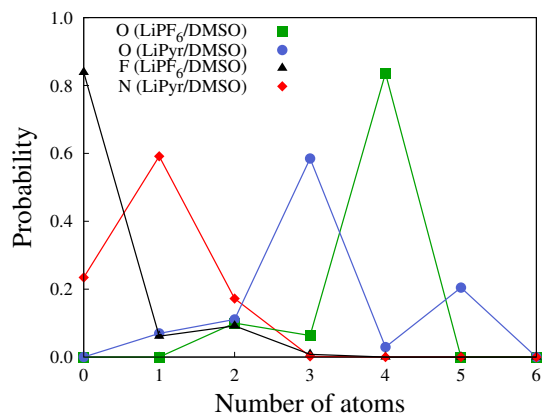
(c)

Fig. 11 Solvation: (a) Li$^+$ coordination numbers for the first shell shown in Figures 9 and 10 as function of molality at 298 K (Experimental data taken from [55] are also shown), and (b) as function of temperature for solutions with 1 mol·kg^{-1}, (c) probability distribution of Li$^+$ coordination environment in the first solvation shell for O from DMSO, F from PF$_6^-$, and N for Pyr$^-$ at 1 mol·kg^{-1} and 298 K.
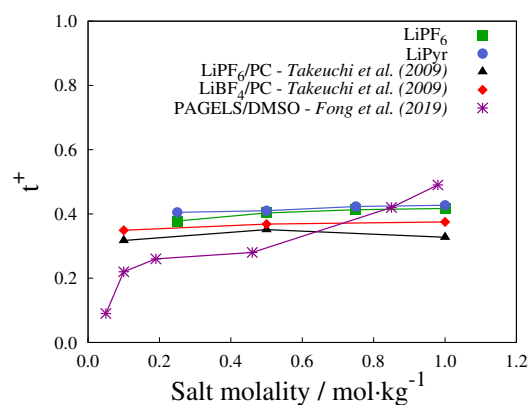

Fig. 12 The Li$^+$ transference number (t^+) for LiPF$_6$ and LiPyr in DMSO solutions at 1 atm and 298 K for different molalities calculated from Green-Kubo diffusivity. Uncertainties are on the order of $\pm$ 0.0001 for all results. Experimental measurements for LiPF$_6$ and LiBF$_4$ in PC [14] and, simulation results for poly(allylglycidyl ether-lithium sulfonate) (PAGELS) in DMSO [58] are also shown for comparison purposes.

19 L. F. M. Franco, M. Castier and I. G. Economou, *J. Chem. Theory Comput.*, 2016, **12**, 5247–5255.

20 I. N. Tsimpanogiannis, O. A. Moultos, L. F. M. Franco, M. B. M. Spera, M. Erdős and I. G. Economou, *Mol. Sim.*, 2016, **45**, 425–453.

21 M. L. Strader and S. E. Feller, *J. Phys. Chem. A*, 2002, **106**, 1074–1080.

22 N. Kumar and J. M. Seminario, *J. Phys. Chem. C*, 2016, **120**, 16322–16332.

23 R. Jorn, R. Kumar, D. P. Abraham and G. A. Voth, *J. Phys. Chem. C*, 2013, **117**, 3747–3761.

24 H. Liu and E. Maginn, *J. Chem. Phys.*, 2013, **139**, 114508.

25 L. Martínez, R. Andrade, E. G. Birgin and J. M. Martínez, *J. Comput. Chem.*, 2009, **30**, 2157–2164.

26 S. Plimpton, *J. Comput. Phys.*, 1995, **117**, 1 – 19.

27 G. J. Martyna, D. J. Tobias and M. L. Klein, *J. Chem. Phys.*, 1994, **101**, 4177–4189.

28 W. Shinoda, M. Shiga and M. Mikami, *Phys. Rev. B*, 2004, **69**, 134103.

29 M. Parrinello and A. Rahman, *J. App. Phys.*, 1981, **52**, 7182–7190.

30 R. Hockney, *Computer simulation using particles*, A. Hilger, Bristol England Philadelphia, 1988.

31 E. J. Maginn, R. A. Messerly, D. J. Carlson, D. R. Roe and J. R. Elliott, *LiveCoMS*, 2019, **1**, 1–20.

32 Y. Zhang, A. Otani and E. J. Maginn, *J. Chem. Theory Comput.*, 2015, **11**, 3537–3546.

33 M. S. Green, *J. Chem. Phys.*, 1953, **22**, 398–413.

34 R. Kubo, *J. Phys. Soc. Jpn.*, 1957, **12**, 570–586.

35 B. L. Holian and D. J. Evans, *J. Chem. Phys.*, 1983, **78**, 5147–5150.

36 B. Hess, *J. Chem. Phys.*, 2002, **116**, 209–217.

37 C. Rey-Castro and L. F. Vega, *J. Phys. Chem. B*, 2006, **110**, 14426–14435.

38 D. Frenkel and B. Smit, *Understanding Molecular Simulation: From Algorithms to Applications*, Academic Press, San Diego, 2nd edn., 2002, vol. 1.

39 I. C. Yeh and G. Hummer, *J. Phys. Chem. B*, 2004, **108**, 15873–

41 B. Dünweg and K. Kremer, *J. Chem. Phys.*, 1993, **99**, 6983–6997.

42 H. Liu and E. Maginn, *J. Chem. Phys.*, 2011, **135**, 1–16.

43 M. S. Alam, B. Ashokkumar and A. M. Siddiq, *J. Mol. Liq.*, 2019, **281**, 584–597.

44 L. de Pablo, J. J. Segovia, A. Martín, M. C. Martín and M. D. Bermejo, *J. Chem. Thermodyn.*, 2018, **123**, 185–194.

45 M. Morita, F. Tachihara and Y. Matsuda, *Electrochim. Acta*, 1987, **32**, 299–305.

46 U. Weinert and E. A. Mason, *Phys. Rev. A*, 1980, **21**, 681–690.

47 J. A. Padró, J. Trullàs and G. Sesé, *Mol. Phys.*, 1991, **72**, 1035–1049.

48 K. Harris, *J. Phys. Chem. B*, 2010, **114**, 9572–9577.

49 P. Walden, *Z. Phys. Chem.*, 1906, 207–249.

50 K. Harris, *J. Phys. Chem. B*, 2019, **123**, 7014–7023.

51 C. Schreiner, S. Zugmann, R. Hartl and H. J. Gores, *J. Chem. Eng. Data*, 2010, **55**, 1784–1788.

52 W. Xu, E. I. Cooper and C. A. Angell, *J. Phys. Chem. B*, 2003, **107**, 6170–6178.

53 I. Gunasekara, S. Mukerjee, E. J. Plichta, M. A. Hendrickson and K. M. Abrahama, *J. Electrochem. Soc.*, 2014, **161**, A381–A392.

54 A. Alsudairi, A. Lajami, I. Kendrick, S. Mukerjee and A. K. M., *J. Electrochem. Soc.*, 2019, **166**, A305–A317.

55 Y. Yamada, Y. Takazawa, K. Miyazaki and T. Abe, *J. Phys. Chem. C*, 2010, **114**, 11680–11685.

56 N. Mozhzhukhina, M. P. Longinotti, H. R. Corti and E. J. Calvo, *Electrochim. Acta*, 2015, **154**, 456–461.

57 K. M. Diederichsen, E. J. McShane and B. D. McCloskey, *ACS Energy Lett.*, 2017, **2**, 2563–2575.

58 K. D. Fong, J. Self, K. M. Diederichsen, B. M. Wood, B. D. McCloskey and K. A. Persson, *ACS Cent. Sci.*, 2019, **5**, 1250–1260.

59 V. S. Dilimon, C. Hwang, Y. G. Cho, J. Yang, H. D. Lim, K. Kang, S. J. Kang and H. K. Song, *Sci. Rep.*, 2017, **7**, 1–10.

60 Y. Marcus, *Ions in Solution and their Solvation*, 2015, pp. 1–293.

61 K. M. Abraham, *J. Electrochem. Soc.*, 2015, **162**, A3021–A3031.

62 M. Schmeisser, P. Illner, R. Puchta, A. Zahl and R. Van Eldik, *Chem. Eur. J.*, 2012, **18**, 10969–10982.
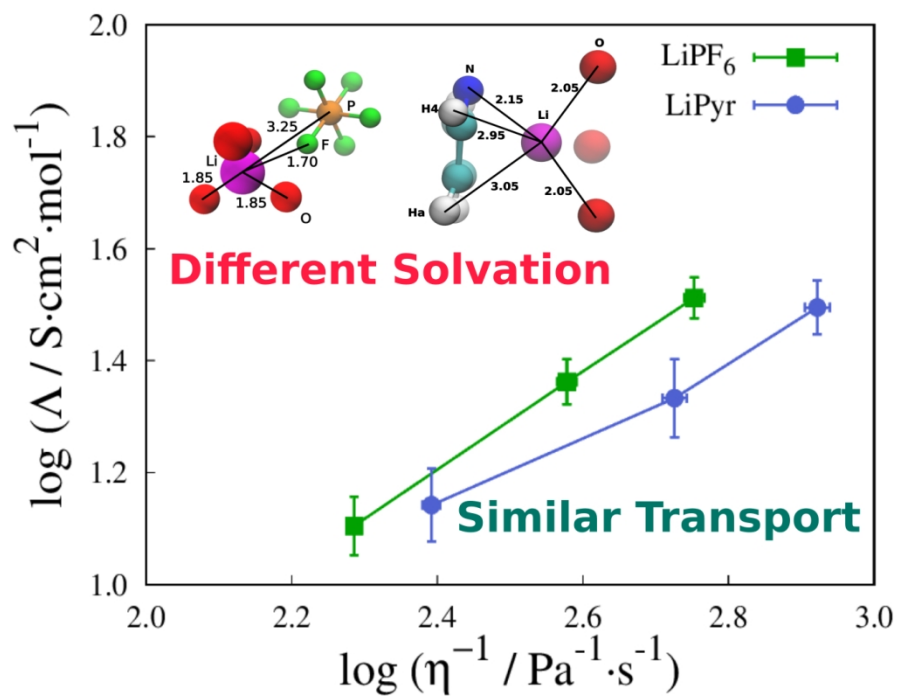
In this study we investigate, via molecular dynamic, transport properties and structural features of two lithium salts with different anions shape (LiPF6 and LiPyr in DMSO). We found that, despite similar conductivities, the solvation structure can be quite different.